Electromagnetic Induction Imaging at Multiple Depths With a Single Coil

Mahindra Ganesh, Maryam Ravan, *Senior Member, IEEE*, and Reza K. Amineh, *Senior Member, IEEE*

***Abstract*— Electromagnetic induction imaging (EII) is an attractive imaging modality due to its contactless operation, low cost, and good penetration depth. To implement real-time imaging, in applications such as object tracking or functional biomedical imaging, fast data acquisition is required. To proceed toward this goal, in this article, we propose the use of a single coil for 3-D EII along with a fast inversion approach. To collect sufficient data that allow 3-D imaging, we propose two approaches: collecting data at multiple coil's drive current levels and collecting data with multiple tank circuit's capacitor values. We show that the use of such data when using a single coil allows for 3-D EII. For proof-of-concept experiments, we use a commercial data acquisition board, that is, LDC1614EVM module, and multilayer planar coils made by Texas Instruments.**

***Index Terms*— Electromagnetics, eddy currents, imaging and sensing, inductive sensing.**

I. Introduction

ELECTROMAGNETIC induction imaging (EII) [1] is a technique for imaging of conductive objects. In EII, a magnetic field is generated by a current-carrying coil. This field induces eddy currents in the objects. These currents, in turn, produce a secondary magnetic field which is measured by the same coil or a receiver coil. It is this secondary magnetic field that carries information about the shape, size, and location of the objects. The main advantages of using EII include: 1) noncontact operation; 2) good penetration; 3) cost-effectiveness compared with microwave [2] and millimeter-wave [3] technologies; and 4) sensitivity to all three electromagnetic properties: conductivity, permittivity, and permeability [4]. Due to these advantages, EII has gained significant attraction in various applications, including imaging of metallic objects (see [5]–[7]), biomedical imaging (see [8]–[17]), nondestructive testing (see [18]–[20]), and national nuclear security (see [21]).

Here, we first briefly review the eddy current testing (ECT) techniques in terms of the utilized spectral content. In ECT techniques, the use of single-frequency excitation [22] limits the operation to single depth sensing. To obtain resolution along the depth, multiple-frequency ECT techniques [23] have been developed with simultaneous or sequential excitations. The simultaneous excitation approach is faster and requires less power in each frequency component compared with the sequential excitation. On the other hand, the frequency sweep approach [24] allows for data collection over a broad bandwidth leading to higher depth resolutions. However, sweeping the frequency increases the duration of data acquisition process. Pulsed ECT technique [25] using a wide bandwidth solves this issue, leading to shorter data collection times for multiple depth inspections. Furthermore, the use of wireless power transfer concepts along with multiple resonant frequencies and their relevant responses has shown promising results for multiple depth inspections [26].

Furthermore, in the following, we review some of the main EII configurations. In [15], a two-coil system has been proposed, in which the imaged object was scanned between the coils. The system operated at 2 MHz and the receiver coil formed a resonant circuit together with the capacitance of the cables and circuitry. In [1] a multiple pole system was developed at 100 kHz. Sixteen transmitter/receiver coils were wound on cores that were mounted on a ferrite rod surrounding the imaged domain. This avoided the need for mechanical scanning. The system had a magnetic shield to concentrate the field inside the imaged domain, increase sensitivity, and reduce susceptibility to interferences. In [27], a 500 kHz system has been proposed to increase the sensitivity at the center of the imaged domain. The system was composed of four parts: transmitter coils, receiver coils, a magnetic confinement screen, and an external conducting screen. The transmitter coil consisted of two pairs of orthogonal windings surrounding the imaged domain to ensure generation of a parallel uniform magnetic field inside the imaged domain. The system proposed in [28], contained 16 transmitter and receiver coils along with their transceiver modules. The transmitter and receiver coils were reeled up in pairs on cylindrical formers and placed along a circular imaged domain. In EII systems, the large primary field signal limits the accuracy with which the small in-quadrature secondary signal can be measured. To avoid this shortcoming, the use of back-off coils [4] and gradiometers [29]–[32] has been investigated, which reduces the sensitivity of the measurement coils to the primary field. Data collection by scanning a single gradiometer [33] or using a planar-array scheme [34], [35] has been studied. Along biomedical imaging applications, in [36], the better sensitivity distribution of the hemispherical arrangement for the coils

Manuscript received October 5, 2020; revised December 23, 2020; accepted December 31, 2020. Date of publication January 11, 2021; date of current version January 27, 2021. This work was supported in part by the U.S. National Science Foundation (NSF) under Grant 1920098 and in part by the New York Institute of Technology's Institutional Support for Research and Creativity (ISRC) Grants. The Associate Editor coordinating the review process was Zheng Liu. *(Corresponding author: Reza K. Amineh.)*

The authors are with the Department of Electrical and Computer Engineering, New York Institute of Technology, New York, NY 10023 USA (e-mail: rkhalaja@nyit.edu).

Digital Object Identifier 10.1109/TIM.2021.3050659

was confirmed. Construction of a 15-channel hemispherical helmet-shaped EII device for brain imaging was also reported in [10]. Furthermore, in [16], detecting a cerebral hemorrhage has been proposed with a hemispherical coil array of 56 transmitter/receiver coils operating at 1 and 10 MHz.

For higher dynamic range in an EII system, resonant-based measurement systems have been used. In [19], Q-detection sensors have been used for inspection of steel reinforcing bars in concrete. In [37] and [38], *LC* resonance systems have been proposed for detection of metallic wear debris in rotating and reciprocating machinery. In [39], 2-D EII has been proposed with the use of a resonant LCR circuit for imaging of metallic samples. It has been extended in [40], for imaging of similar samples covered by conductive barriers.

So far, attempts have been made to implement fast 3-D EII. Most notably, in [41], a planar array of 4×4 coils has been used for this purpose and a linear inverse solver together with the Tikhonov regularization has been used for imaging. There, the depth information has been obtained via the use of nonadjacent coils. Recently, in [42], a fast and robust approach has been proposed for 3-D EII. There, the assumptions that the imaging system is linear and space-invariant led to the development of a fast inversion approach based on the use of convolution theory. In [42], the depth resolution has been achieved via the use of multiple coils with various parameters and the data acquisition has been implemented via raster scanning of the coils which is slow. This prevents the use of such system in real-time or quasi real-time applications such as object tracking or functional biomedical imaging. These applications demand for fast data acquisition, for instance, by electronically scanning an array of sensors. The spatial limitations for a sensor array necessitate achieving depth resolution via the use of a single coil.

Thus, to bridge the above-mentioned gap, in this article, we propose the use of a single coil along with multiple coil's drive current levels or multiple resonant capacitor values to achieve depth resolution with a single sensor. Although we still use raster scanning of the coil for proof-of-concept experiments, we demonstrate that the collected data are sufficient for 3-D EII, paving the way toward construction of an electronically scanned array of coils. The performance of the proposed techniques will be validated through experiments, and the quality of the reconstructed images is compared using a quantitative measure.

II. Theory

Fig. 1 illustrates the proposed imaging setup. It includes a transceiver coil connected in parallel with a capacitor to provide an *LC* tank circuit for high dynamic range measurements. In such a system, the presence of the objects under test (OUTs) can be sensed via the measurement of the resonant frequency of the tank circuit since the presence of the OUTs changes the equivalent inductance of the coil leading to a change in the resonant frequency of the corresponding *LC* tank circuit. From now on, we refer to this measured resonant frequency change as the "response." Here, we propose data acquisition with a single coil but at N_I levels for the drive current I_d and N_c different values for the resonant capacitor C. For this purpose, at each sampling position (x, y), the responses are acquired at all the current levels and all capacitor values. Then, we aim at reconstructing images over the $z = z_i$ planes for $i = 1, \ldots, N_z$.

Similar to [42], assuming that the system is linear and space-invariant, we use convolution theory, that is, the OUTs' response is considered as the convolution of the point-spread function (PSF) of the system and the spatial shape function (contrast function) of the OUTs. The PSF of the system is approximated by the response for the smallest measurable OUT placed at the origin of the *xy plane* representing a Dirac delta function. We call these small OUTs calibration objects (COs).

To obtain the PSF data, we collect the responses $R_i^{\text{co}}(x, y, I_j, C_k)$ at each drive current level I_j, $j = 1, \ldots, N_I$ and capacitor value C_k, $k = 1, \ldots, N_C$ due to the COs placed, one at a time, at $(0, 0, z_i)$, $i = 1, \ldots, N_{z,}$. The total response $R(x, y, I_j, C_k)$ due to the OUTs can then be approximated with the superposition of the OUT responses corresponding to each plane. The OUT response at each plane, in turn, can be written as the convolution of the measured PSF at that plane $R_i^{\text{co}}(x, y, I_j, C_k)$ with the spatial shape of the OUTs on the corresponding plane $c_i(x, y)$. Thus, $R(x, y, I_j, C_k)$ can be written as

$$R(x, y, I_j, C_k) \approx \sum_{i=1}^{N_z} R_i^{\text{co}}(x, y, I_j, C_k) *_x *_y c_i(x, y). \quad (1)$$

In (1), $R_i^{\text{co}}(x, y, I_j, C_k)$ and $R(x, y, I_j, C_k)$ functions are known due to the measurement of the COs and OUTs responses, respectively. To estimate $c_i(x, y)$ functions, the responses are acquired at N_I levels for the drive current I_d and N_c different values for the resonant capacitor C. Thus, the following system of equations can be constructed (using $\mathbf{s} = (x, y)$ for brevity):

$$\begin{cases} R(\mathbf{s}, I_1, C_1) = \displaystyle\sum_{i=1}^{N_z} R_i^{\text{co}}(\mathbf{s}, I_1, C_1) *_x *_y c_i(\mathbf{s}) \\ \quad \vdots \\ R(\mathbf{s}, I_{N_I}, C_1) = \displaystyle\sum_{i=1}^{N_z} R_i^{\text{co}}(\mathbf{s}, I_{N_I}, C_1) *_x *_y c_i(\mathbf{s}) \\ \quad \vdots \\ R(\mathbf{s}, I_1, C_{N_C}) = \displaystyle\sum_{i=1}^{N_z} R_i^{\text{co}}(\mathbf{s}, I_1, C_{N_C}) *_x *_y c_i(\mathbf{s}) \\ \quad \vdots \\ R(\mathbf{s}, I_{N_I}, C_{N_C}) = \displaystyle\sum_{i=1}^{N_z} R_i^{\text{co}}(\mathbf{s}, I_{N_I}, C_{N_C}) *_x *_y c_i(\mathbf{s}) \end{cases} \quad (2)$$

For solving the system of equations in (2), 2-D Fourier transforms (with respect to the x and y variables) are applied on both sides of the equations leading to the following system of equations at each spatial frequency pair (here, we use $\boldsymbol{k} = (k_x, k_y)$ for brevity, where k_x and k_y are the Fourier

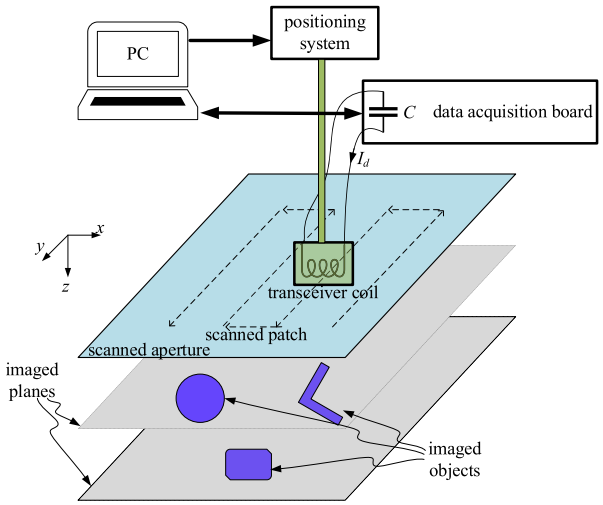

Fig. 1. Illustration of the EII setup.

variables corresponding to the x and y variables, respectively):

$$\begin{cases} \tilde{\tilde{R}}(\boldsymbol{k}, I_1, C_1) = \sum_{i=1}^{N_z} \tilde{\tilde{R}}_i^{\mathrm{co}}(\boldsymbol{k}, I_1, C_1)\tilde{\tilde{c}}_i(\boldsymbol{k}) \\ \vdots \\ \tilde{\tilde{R}}(\boldsymbol{k}, I_{N_I}, C_1) = \sum_{i=1}^{N_z} \tilde{\tilde{R}}_i^{\mathrm{co}}(\boldsymbol{k}, I_{N_I}, C_1)\tilde{\tilde{c}}_i(\boldsymbol{k}) \\ \vdots \\ \vdots \\ \tilde{\tilde{R}}(\boldsymbol{k}, I_1, C_{N_C}) = \sum_{i=1}^{N_z} \tilde{\tilde{R}}_i^{\mathrm{co}}(\boldsymbol{k}, I_1, C_{N_C})\tilde{\tilde{c}}_i(\boldsymbol{k}) \\ \vdots \\ \tilde{\tilde{R}}(\boldsymbol{k}, I_{N_I}, C_{N_C}) = \sum_{i=1}^{N_z} \tilde{\tilde{R}}_i^{\mathrm{co}}(\boldsymbol{k}, I_{N_I}, C_{N_C})\tilde{\tilde{c}}_i(\boldsymbol{k}) \end{cases} \tag{3}$$

where $\tilde{\tilde{R}}(\boldsymbol{k}, I_j, C_k)$, $\tilde{\tilde{R}}_i^{\mathrm{co}}(\boldsymbol{k}, I_j, C_k)$, and $\tilde{\tilde{c}}_i(\boldsymbol{k})$ are the 2-D Fourier transforms of the functions $R(x, y, I_j, C_k)$, $R_i^{\mathrm{co}}(x, y, I_j, C_k)$, and $c_i(x, y)$, respectively. The system of equations at each $\boldsymbol{k}$ shown in (3) can be solved using beamspace transformation [43].

Using beamspace transformation allows for dimension reduction by designing a transformation to focus on each imaged plane, that is, $z = z_i$ plane, one at a time. For this purpose, we first re-write (3) at each $\boldsymbol{k}$ in a matrix form as

$$\mathbf{b}(\boldsymbol{k}) = \mathbf{A}(\boldsymbol{k})\mathbf{x}(\boldsymbol{k}) \tag{4}$$

where

$$\mathbf{b}(\boldsymbol{k}) = \begin{bmatrix} \tilde{\tilde{R}}(\boldsymbol{k}, I_1, C_1) \\ \vdots \\ \tilde{\tilde{R}}(\boldsymbol{k}, I_{N_I}, C_1) \\ \vdots \\ \tilde{\tilde{R}}(\boldsymbol{k}, I_1, C_{N_C}) \\ \vdots \\ \tilde{\tilde{R}}(\boldsymbol{k}, I_{N_I}, C_{N_C}) \end{bmatrix}, \quad \mathbf{x}(\boldsymbol{k}) = \begin{bmatrix} \tilde{\tilde{c}}_1(\boldsymbol{k}) \\ \vdots \\ \tilde{\tilde{c}}_{N_z}(\boldsymbol{k}) \end{bmatrix} \tag{5}$$

$$\mathbf{A}(\boldsymbol{k}) = \begin{bmatrix} \tilde{\tilde{R}}_1^{\mathrm{co}}(\boldsymbol{k}, I_1, C_1) & \cdots & \tilde{\tilde{R}}_{N_z}^{\mathrm{co}}(\boldsymbol{k}, I_1, C_1) \\ \vdots & \ddots & \vdots \\ \tilde{\tilde{R}}_1^{\mathrm{co}}(\boldsymbol{k}, I_{N_I}, C_1) & \cdots & \tilde{\tilde{R}}_{N_z}^{\mathrm{co}}(\boldsymbol{k}, I_{N_I}, C_1) \\ & \vdots & \\ \tilde{\tilde{R}}_1^{\mathrm{co}}(\boldsymbol{k}, I_1, C_{N_C}) & \cdots & \tilde{\tilde{R}}_{N_z}^{\mathrm{co}}(\boldsymbol{k}, I_1, C_{N_C}) \\ \vdots & \ddots & \vdots \\ \tilde{\tilde{R}}_1^{\mathrm{co}}(\boldsymbol{k}, I_{N_I}, C_{N_C}) & \cdots & \tilde{\tilde{R}}_{N_z}^{\mathrm{co}}(\boldsymbol{k}, I_{N_I}, C_{N_C}) \end{bmatrix}. \tag{6}$$

Hereafter, we omit the notation $(\boldsymbol{k})$ for brevity. The beamspace transformation is implemented using the $(N_C N_I) \times 1$ matrix $\mathbf{T}$ and obtaining the $M < (N_C N_I)$ dimensional beamspace data vectors as $\mathbf{b}_{\mathrm{T}} = \mathbf{T}'\mathbf{b}$, where the prime symbol denotes the Hermitian transpose of a matrix. The columns of $\mathbf{T}$ are assumed to be orthonormal. To determine matrix $\mathbf{T}$, we minimize the average error between the original and beamspace representation of the solution in (4). The beamspace transformed data can be considered as the data in the space spanned by the columns of $\mathbf{T}$. Therefore, the component that is neglected in beamspace is the projection of the data onto the space orthogonal to $\mathbf{T}$ which is $(\mathbf{I} - \mathbf{T}\mathbf{T}')\mathbf{b}$. Accordingly, the squared error related to the mapping an object on the imaged plane z_i, $i = 1, \ldots, N_z$ into the beamspace is

$$e_{\mathbf{T}}^2(i) = \left\|(\mathbf{I} - \mathbf{T}\mathbf{T}')\mathbf{A}_i\right\|_2^2 \tag{7}$$

where $\mathbf{A}_i$ is the ith column of $\mathbf{A}$. To minimize the error for all the imaged planes, matrix $\mathbf{T}$ needs to be selected appropriately. One approach is based on minimizing the error (7) over each plane

$$\min_{\mathbf{T}}\left(e_{\mathbf{T}}^2(i)\right). \tag{8}$$

The problem in (8) is equivalent to a maximization problem as

$$\max \operatorname{tr}(\mathbf{T}'\mathbf{G}\mathbf{T}) \text{ s.t } \mathbf{T}'\mathbf{T} = \mathbf{I} \tag{9}$$

where

$$\mathbf{G} = \mathbf{A}_i\mathbf{A}'_i, \quad i = 1, 2, \ldots, N_z. \tag{10}$$

We select the columns of matrix $\mathbf{T}$ as the eigenvectors corresponding to the M largest eigenvalues of the matrix $\mathbf{G}$. Then, the minimum error in (7) is obtained by the sum of the $(N_C N_I) - M$ smallest eigenvalues of $\mathbf{G}$. Here, the dimension of $\mathbf{A}_i$ is $(N_C N_I) \times 1$. This leads to a rank of one for matrix $\mathbf{G}$ $(M = 1)$. Thus, matrix $\mathbf{T}$ is reduced to a vector, that is, the eigenvector corresponding to the largest eigenvalue.

The beamspace transformation algorithm needs to be applied at each $\boldsymbol{k}$ to solve the corresponding system of equations. For this purpose, the matrix $\mathbf{A}$ must also be transformed as

$$\mathbf{A}_{\mathrm{T}} = \mathbf{T}'\mathbf{A}. \tag{11}$$

Then, a system of equations need to be solved as

$$\mathbf{b}_{\mathrm{T}} = \mathbf{A}_{\mathrm{T}}\mathbf{x} \tag{12}$$

at each $\boldsymbol{k}$ to estimate $\tilde{\tilde{c}}_i(\boldsymbol{k})$ at the imaged plane $z = z_i$. The solution approach described above has to be implemented N_z times to estimate $\tilde{\tilde{c}}_i(\boldsymbol{k})$ functions. It is worth noting that since $\mathbf{G} = \mathbf{A}_i\mathbf{A}'_i$, $\mathbf{T}$ is proportional to $\mathbf{A}_i$. Hence, the left-hand

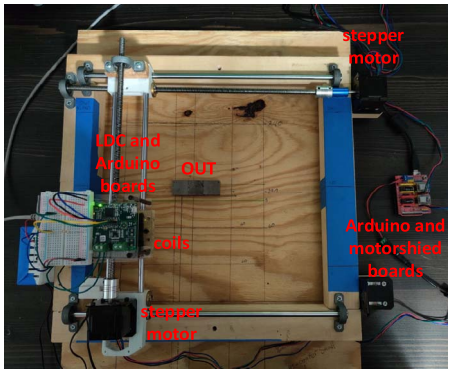

Fig. 2. Photograph of the imaging setup.

side of the transformed equation (12) becomes the inner product of $\mathbf{A}'_i\mathbf{b}$, and the coefficient matrix on the right-hand side becomes $\mathbf{A}'_i\mathbf{A}$. Therefore, the resulting $\tilde{\tilde{c}}_i(\boldsymbol{k})$ can be considered as $(\mathbf{A}'_i\mathbf{A})^+(\mathbf{A}'_i\mathbf{b})$, where the superscript "+" denotes matrix pseudoinverse.

After solving the systems of equations for all $\boldsymbol{k}$, inverse 2-D Fourier transform is applied to $\tilde{\tilde{c}}_i(\boldsymbol{k})$ functions to reconstruct 2-D images $c_i(\mathbf{s})$. For final visualization, the normalized magnitude of each $c_i(\mathbf{s})$ function, $|c_i(\mathbf{s})|/L$, where L is the maximum of $|c_i(\mathbf{s})|$ for all z_i, is plotted which represents the 2-D image of the OUTs at the $z = z_i$ plane. The collection of these 2-D slice images is considered as a 3-D image.

III. Imaging Results

To validate the proposed methods of imaging OUTs at various depths, we use an apparatus shown in Fig. 2. It consists of two NEMA 17 stepper motors, two Arduino UNO, a CNC motor shield with DRV8825 drivers, and a Texas Instruments LDC1614EVM evaluation module [44], [45]. The CNC motor shield and DRV8825 drivers are selected for precise control of the positioning system to implement the raster scanning process. The inductive sensors that are used in the first set of experiments consist of two supplied coils for the LDC1614EVM module (we refer to them as small coils). For the second set of experiments, we use Coil H from the LDCCOILEVM kit [46] (we refer to that as large coil). Table I shows the parameters of these coils. The use of two identical small coils with different capacitor values allows for an easy proof-of-concept study of the effect of varying the capacitor values without the need to make a capacitor switching network when using a single coil. Thus, when using the small coils, the LDC1614EVM module is altered to have two different resonant frequencies of 2.812 and 9.327 MHz. Channel 0 (CH0) uses a 30 pF capacitor to acquire a resonant frequency of 9.327 MHz and channel 1 (CH1) uses the supplied 330 pF capacitor to resonate at 2.812 MHz. When using the large coil, we do not use a capacitor for the tank circuit. Instead, we exploit the coil's parasitic capacitance to resonate at 7.8 MHz. Fig. 3 shows the two identical small coils with different capacitor values. It also shows the large coil.

The 2-D scanned area in all the experiments has dimensions of 200 mm × 200 mm with sampling steps of 10 mm in both the x and y directions. The imaged OUTs are steel cubes with dimensions of 23 mm × 24 mm × 15 mm. The depth of an object is measured as the distance from the surface of the coil sensor downward to the top surface of the OUT.

TABLE I
Parameters of the Used Coils

Coil	Diameter (mm)	Turns per Layer	Trace Width (mm)	Trace Spacing (mm)	No. of Layers
Small coils	13.9	19	0.15	0.15	2
Large coil	46	50	0.15	0.15	2

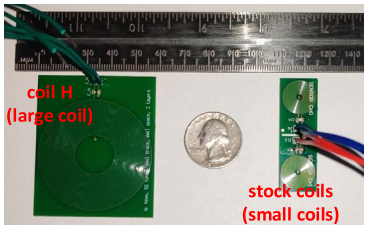

Fig. 3. Photograph of the used coils, i.e., the supplied coils with the LDC1614EVM module (small coils) and the Coil H (large coil).

A. Configuration of the LDC1614EVM Module

To change the drive current level I_d for a coil, we configure the LDC1614EVM module according to the reference document provided by Texas Instruments [45] (summarized in Table II). As per instructions, we need to first determine the OUT distance, the factor of resolution, and the used sensor. For the used sensor, we set the channel divider as per the reference document and the sensor's frequency. The resonant frequencies of the small sensors are smaller than 10 MHz. The settling count register which indicates a stabilized measurement is set using the following formula to minimize the noise:

$$\text{SETTLECOUNT}_i > \frac{Q f_{\text{REF}_i}}{16 f_{\text{SENSOR}_i}} \tag{13}$$

where subscript i denotes the channel number (0 or 1), Q is the quality factor for the sensor, f_{SENSOR_i} is the resonant frequency of the ith channel, and f_{REF_i} is the reference frequency for the internal or external oscillator used in the LDC1614EVM's core to measure the sensors' frequency. The LDC1614EVM has a maximum internal reference frequency of 40 MHz for a single sensor and 35 MHz for a dual sensor. The digitized output for each channel is proportional to the ratio of $f_{\text{SENSOR}}/f_{\text{REF}}$.

For the case that we use two small sensors with different capacitor values, a channel switching delay of 1 μs was used for the reference frequency of 21.7 MHz based on a divider code of 2. In our Arduino code, we also included a delay of 250 ms after each programming of the sensor for further stabilization.

Next, the reference count for channel i, $R\text{COUNT}_i$, is programmed to determine the conversion resolution (a longer conversion time t_{co} provides a higher resolution for the measurement) as

$$t_{\text{co}i} = \frac{16\text{RCOUNT}_i}{f_{\text{REF}_i}}. \tag{14}$$

According to the reference document, we use decimal value of 1238 for RCOUNT_i.

TABLE II
INITIAL CONFIGURATION OF REGISTERS FOR LDC1614EVM MODULE

Address	Value	Register Name	Comments
0x08	FFFF	RCOUNT0	For CH0 with max resolution of 65535
0x09	FFFF	RCOUNT1	For CH1 with Max resolution of 65535
0x10	0610	SETTLECOUNT0	For CH0, Settling Time 1552us
0x11	0610	SETTLECOUNT1	For CH1, Settling Time 1552us
0x14	1002	CLOCK_DIVIDERS0	For CH0, FIN_DIVIDER=01 For CH0, FREF_DIVIDER=10
0x15	1002	CLOCK_DIVIDERS1	For CH1, FIN_DIVIDER=01 For CH1, FREF_DIVIDER=10
0x19	0000	ERROR_CONFIG	0000
0x1B	820D	MUX_CONFIG [30pF]	AUTOSCAN_EN - b1 [Sequential Mode] RR_SEQUENCE - b00 [CH0 CH1] DEGLITCH - 10 MHz
0x1B	820C	MUX_CONFIG [330pF]	AUTOSCAN_EN - b0 [Continuous Mode] RR_SEQUENCE - b00 [CH0 CH1] DEGLITCH – b100 - 3.3 MHz
0x1E	0800	DRIVE_CURRENT0	For CH0, C0 – 18uA
0x1F	0800	DRIVE_CURRENT1	For CH1, C0 – 18uA
0x1A	1401	CONFIG	ACTIVE_CHAN - b00 [Perform continuous conversion on channel 0] SLEEP_MODE_EN - b0 [Active], RP_OVERRIDE_EN - b1 [Rp Override On] SENSOR_ACTIVATE_SEL - b0 [Full Current Activation Mode] AUTO_AMP_DIS - b1 [Automatic Amplitude Correction is disabled] REF_CLK_SRC - b0 [Use internal oscillator as reference frequency] INTB_DIS - b0 [INTB pin will be asserted when status register updates] HIGH_CURRENT_DRV - b0 [The LDC will drive all channels with normal sensor current]

The ERROR_CONFIG register was not used and was set to a binary value of 0000.

The drive current levels for the ith channel can be changed through the CH_i_IDRIVE register (selected from the 32 possible fixed values). To change the current, after programming of the initial registers, the line drop compensator (LDC) is programmed into the sleep mode. Then, the current register is written and the LDC is programmed back into the normal mode (the LDC registers can only be programmed in the sleep mode). At each sampling position, the data are collected at four drive current levels at 424, 736, 1173, and 1563 μA for each used coil.

Following the programming of CH_i_IDRIVE register, we program the MUX_CONFIG register which deals with the configuration of the data acquisition setup. AUTOSCAN_EN is set to a binary 0 to enable continuous mode for a single-sensor setup (when using the large coil) and a binary 1 is used to enable sequential mode for multiple sensors (when using small coils). The RR_SEQUENCE field of the MUX_CONFIG was set to a binary value of 00 for both single- and dual-sensor setup on CH0 and CH1. Finally, one of the most important characteristics of the MUX_CONFIG that needs to be set appropriately is the DEGLITCH segment. The DEGLITCH field of the MUX_CONFIG is required to filter out noise based on the operating frequency of the sensor. The input DEGLITCH filter bandwidth was selected for the lowest setting that exceeds the maximum sensor oscillation frequency: for the small coil with a 30 pF capacitor, a DEGLITCH value of 10 MHz was used while for the small coil with 330 pF, a DEGLTICH value of 3.3 MHz is used. Finally, for the large coil without a capacitor, a DEGLITCH value of 3.3 MHz is used.

Finally, the CONFIG register is programmed to transition the LDC from the sleep mode to the operational mode. For the CONFIG register, the ACTIVE_CHAN field was set to binary 00 to select channel 0, the MUX_CONFIG.AUTOSCAN_EN determines which channels are selected based on its operational mode, SLEEP_MODE_EN is set to a binary of 0 to enable conversion (setting that to 1 takes the LDC into the sleep mode), RP_OVERRIDE_EN is set to a binary 1 to disable auto-calibration (this is needed to manually set the current levels), SENSOR_ACTIVATE_SEL is set to a binary 0 for a full current drive during sensor activation, AUTO_AMP_DIS field is set to binary 1 to disable auto-amplitude correction so that the raw data readings are not altered after every current change, and finally the REF_CLK_SRC field is set to a binary 0 to use the internal clock source.

After the initial setup of the LDC, we change the current of the sensors by sending a trigger character over serial data from MATLAB to the Arduino. The Arduino code uses various functions that write to the LDC registers to first place the LDC into the sleep mode, and then write the new current levels to its respective register followed by writing to the CONFIG register to bring LDC back into its normal mode. After the LDC is placed into the normal mode, data are read from the register in a buffer variable. After the buffer is read, a delay (the 250 ms delay mentioned before) is applied to allow the sensor reading to stabilize beyond its settling time prior to returning to the main program where the data are once again read and sent back to MATLAB over serial communication port. After all data are read, MATLAB commands the move to the next sampling position.

B. Imaging Results for Small Coils

The first set of experiments are conducted with the small coils connected at channels CH0 and CH1 of the LDC1614EVM sensor with tank capacitors of 30 and 330 pF, respectively. The drive current levels are changed according to the four levels described before. The two imaged planes are

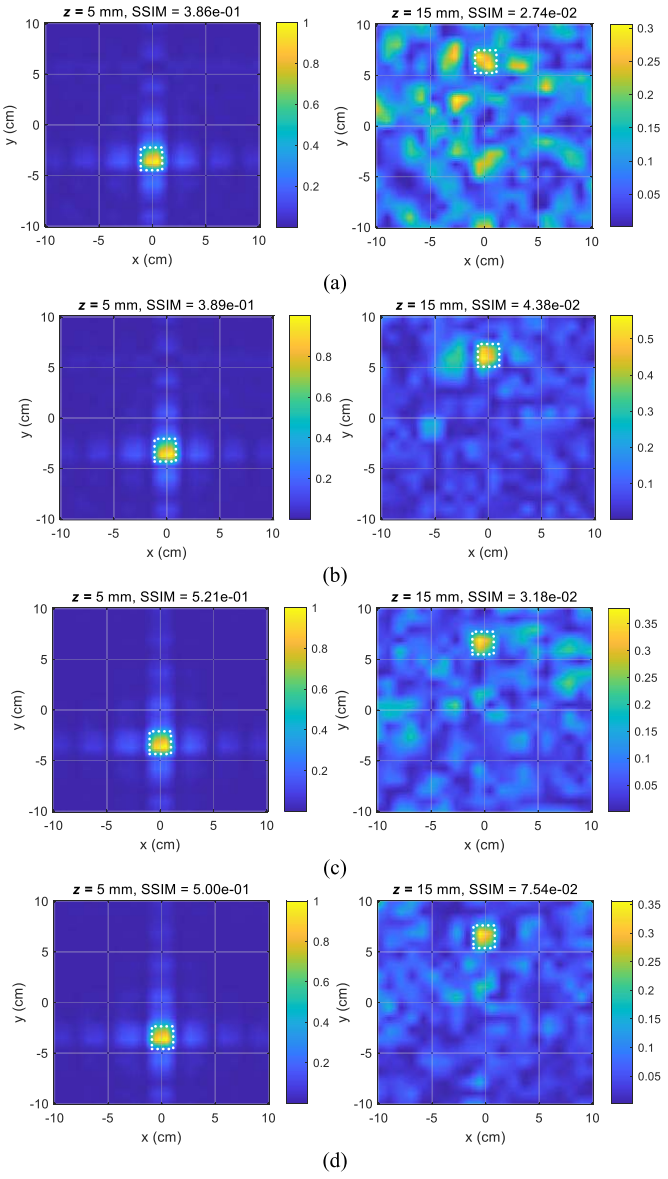

Fig. 4. Reconstructed images at two depths of $z = 5$ and 15 mm with the use of small coils and when using (a) CH1 coil and two drive current levels, (b) CH1 coil and four drive current levels, (c) CH0 and CH1 coils and two current levels, and (d) CH0 and CH1 coils and four current levels. The white dotted lines show the boundaries of the OUTs. The value of the computed SSIM parameter has been provided in the title of each image.

at $z = 5$ and 15 mm. After measuring the PSFs corresponding to COs, we place two OUTs, one at $z = 5$ mm and the second one at $z = 15$ mm.

Fig. 4 shows the reconstructed images for four scenarios to study the effect of increasing the number of drive current levels and the number of capacitor values. Fig. 4(a) shows the images when using data corresponding to only two current levels (minimum and maximum levels) and using CH1 coil only (one capacitor value). Fig. 4(b) shows the images when using the data corresponding to all four current levels but still using CH1 coil only (one capacitor value). Fig. 4(c) shows the images when using the data collected at two current levels (minimum and maximum levels) and using CH0 and CH1 coils (two capacitor values). Finally, Fig. 4(d) shows the images when using the data collected at all four current levels and using CH0 and CH1 coils (two capacitor values).

Here, we use a quantitative metric, called structural similarity (SSIM) index [47], to assess the quality of the reconstructed images. The SSIM parameter is obtained from the product of three terms: luminance term, contrast term, and structural term. Here, this parameter is computed for each reconstructed 2-D image with respect to a reference image of the OUTs (which is zero everywhere except being 1 at the positions of the OUTs). Higher SSIM values are desirable.

By comparing the values of SSIM for various scenarios in Fig. 4, it is observed that the quality of the images improves when using the collected data at larger number of currents and more capacitor values. The quality improvement is more drastic for the deeper imaged plane at $z = 15$ mm. By comparing the SSIM values, it is observed that the quality of the images degrades as the imaging distance increases. The best image quality is achieved when using all the current levels and both capacitor values as expected and demonstrated in Fig. 4(d). One last observation is that the magnitude of the images at $z = 5$ mm is much stronger compared with those at $z = 15$ mm (please refer to the colorbars).

C. Imaging Results for Large Coil

In the previous section, we presented the imaging results for the small coils and studied the effects of the number of drive current levels (N_I) and number of capacitor values (N_C). Two imaged planes were considered at $z = 5$ mm and $z = 15$ mm. We also tried to implement imaging at an additional imaged plane at $z = 25$ mm when using data collected by the small coils but it was not successful. We do not present the results for the sake of brevity. The small sensors even with the maximum drive current level and for both used capacitor values do not show much sensitivity to an OUT at $z = 25$ mm. Thus, we conducted a second set of experiments using the large coil introduced before. This large coil allows for sensing and imaging OUTs at farther distances as we demonstrate in the following.

Fig. 5 shows the reconstructed images using the large coil with four drive current levels and over three imaged planes at $z = 5$, 15, and 25 mm. The three objects distributed over these three planes can be reconstructed correctly in the images although the magnitude of the objects decreases for deeper OUTs as observed in the previous examples as well. Comparing the SSIM values also shows that the quality of the images degrades as the imaging distance increases.

Due to the use of system linearity assumption in deriving (1), the interaction between the OUTs is neglected. This implies that the quality of the proposed inversion technique degrades with the increase in the number, size, and conductivities of the OUTs. To study this degradation, we conduct another imaging experiment with the use of large coil and four drive current levels for that. The imaged planes are similar to the previous example, but this time the OUT is composed of five metal blocks used in the previous experiments attached in a row to make a big "line-shaped" object. This object is placed at the $z = 15$ mm imaged plane and the data acquisition and image reconstruction are implemented as before. Fig. 6 shows

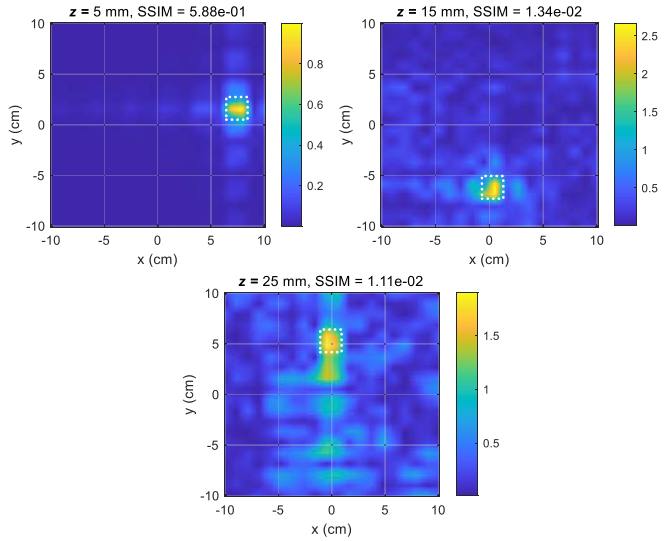

Fig. 5. Reconstructed images at three depths of $z = 5$, 15, and 25 mm, when using Coil H and using four drive current levels. The white dotted lines show the boundaries of the OUTs. The value of the computed SSIM parameter has been provided in the title of each image.

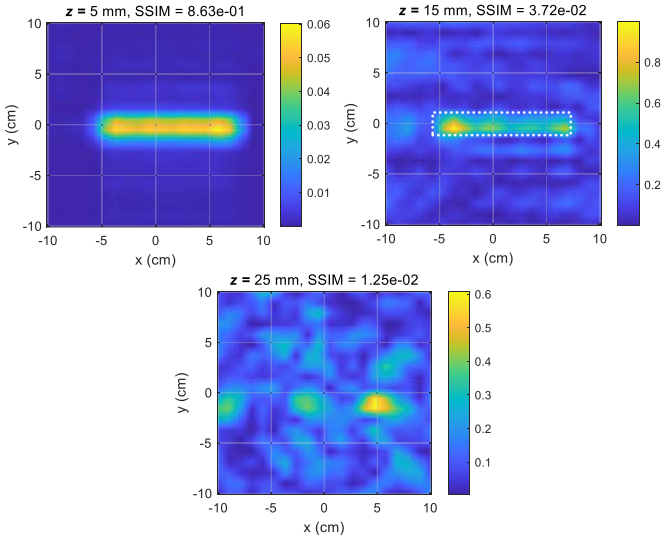

Fig. 6. Reconstructed images of a large object at $z = 15$ mm using the large coil and four drive current levels. The white dotted lines show the boundaries of the OUT. The value of computed SSIM parameter has been provided in the title of each image.

the results of this experiment. It is observed that the object is detected on the corresponding imaged plane. However, a weaker shadow of that is observed at the $z = 5$ mm plane and a stronger artifact is observed on the $z = 25$ mm plane (please refer to the colorbars). This clearly demonstrates the degradation of the image reconstruction results for larger OUTs.

IV. Conclusion and Discussion

In this article, we proposed techniques to achieve 3-D EII of metallic objects when using a single coil along with a fast and robust image reconstruction technique. This allows for proceeding toward building a fast 3-D EII camera based on the use of sensor arrays to expedite the data acquisition process. The depth resolution with a single coil has been achieved by changing either the drive current level for the coil or by changing the capacitor in the corresponding tank circuit or a combination of both techniques. Having a coil with stronger magnetic field (here achieved by larger diameter) allows for imaging objects at larger distances. Obtaining stronger magnetic field for imaging at farther distances can also be achieved via the use of larger number of turns, more layers, or larger drive current levels for the used coil.

A common problem in EII is the relatively small OUTs' responses superimposed on a much larger background response which makes extracting the OUTs' responses challenging. A convenient solution is obtaining and subtracting the background response without physically changing the measurement setup. Practical approaches to estimate the background response include (assuming large scanned aperture compared with the size of the OUTs): 1) sampling the responses in a position far from the OUTs; 2) averaging the responses measured over the scanned aperture; and 3) creating the histogram of the responses and using the response which is the most common.

In the proposed techniques, selecting the range of the spatial Fourier variables' pair $\boldsymbol{k} = (k_x, k_y)$ needs meticulous work. Larger ranges allow for obtaining better lateral spatial resolution for the images and also boost the high-frequency noise. In practice, tuning the range of these variables can be performed for imaging pre-known objects.

In EII techniques, 3-D image reconstruction involves solving a nonlinear inverse problem which is very costly in terms of computational memory and time (see [16]). One common method for more affordable solutions is to linearize the forward problem and optimize the material properties using an iterative optimization technique (see [33], [35], [41], [48]) which is still computationally expensive even with additional simplifications such as breaking the original 3-D problem into several independent 2-D problems. Another common approach is reconstructing the 3D scene slice by slice using back-projection algorithms (see [15], [27], [28]). Each slice is the image of a cross section of the 3-D scene. In addition to the model's linearity assumption, this approach suffers from neglecting the responses of the OUTs on the adjacent 2-D slices. In general, the above-mentioned approaches provide qualitative images. The technique proposed here can be categorized as a qualitative technique as well due to the use of model's linearity assumption. However, the solution process is much faster and less memory consuming compared with the optimization-based techniques, thanks to the breaking of original large system of equations in (2) into many smaller systems of equations in the spatial frequency domain. Besides, the technique is more accurate compared with back-projection-based approaches since the 3-D imaging problem is solved as a whole. In general, linear models have been used extensively in the electromagnetic imaging applications such as the millimeter security screening systems used at the airports (see [49]) which provide striking image resolutions. However, it is well-known that linearity assumptions lead to further degradation of the image quality for larger OUTs (see [50] and [51]). This has been demonstrated by the last example (Fig. 6) in this article.

One main advantage of eddy-current-based techniques is their noncontact operation and their immunity to some environmental influences such as oil and dirt [52]. However, the ripples in the lift-off distance for the sensor, that is, distance between the sensor and the surface of the tested medium, produce undesired effects in their responses [53], [54]. Such ripples that can be due to the tilt, vibration, deformation of samples, and the micro-displacement of the scanning system/operator are difficult to control in industrial settings. Thus, making an array of sensors facilitated by the approaches proposed in this work will be a significant step toward alleviating this problem, in addition to the faster data acquisition process.

As a final note, to compare the diversity of data using the two proposed techniques, we compute the correlation coefficients for the collected PSFs at two current levels or two capacitor values for each depth. The correlation coefficient between the measured PSFs at maximum and minimum current levels for each channel (CH0 or CH1) coil is within the range of 0.2–0.7 at various imaged planes. We believe that these nonunity values are mainly due to the use of ferromagnetic OUTs, the nonlinear properties of which lead to the change in the total coil inductance, the change in resonant frequencies, and thus the change in field distributions when the current level changes. This implies that the technique based on the use of current level works only for imaging of ferromagnetic OUTs. On the other hand, the correlation coefficients between the PSFs measured by CH0 and CH1 coils (different capacitors) are much lower and within the range of 0.01–0.1 (at various current levels and various imaged planes). It is expected since the change in tank circuit's capacitor leads to more drastic change in resonant frequency and the corresponding field distribution for the coil. Overall, our study shows that the change in capacitors can be a more effective approach for obtaining more diverse information and for imaging of a wider range of OUTs.

REFERENCES

[1] A. J. Peyton *et al.*, "An overview of electromagnetic inductance tomography: Description of three different systems," *Meas. Sci. Technol.*, vol. 7, no. 3, pp. 261–271, Mar. 1996.

[2] R. K. Amineh, N. K. Nikolova, and M. Ravan, *Real-Time Three-Dimensional Imaging of Dielectric Bodies Using Microwave/Millimeter Wave Holography*. Hoboken, NJ, USA: Wiley, 2019.

[3] S. Kharkovsky and R. Zoughi, "Microwave and millimeter wave nondestructive testing and evaluation–Overview and recent advances," *IEEE Instrum. Meas. Mag.*, vol. 10, no. 2, pp. 26–38, Apr. 2007.

[4] S. Hermann, "Magnetic induction tomography," *Frontiers Neurosci.*, vol. 4, pp. 1126–1131, 1900.

[5] H. S. Tapp and A. J. Peyton, "A state of the art review of electromagnetic tomography," in *Proc. 3rd World Congr. Ind.Process Tomogr.*, Banff, AB, Canada, 2003, pp. 34–36.

[6] H. Griffiths, *Magnetic Induction Tomography Electrical Impedance Tomography: Methods, History and Applications*, D. S. Holder, Ed. Bristol, U.K.: Institute of Physics Publishing, 2005, pp. 213-238.

[7] B. J. Darrer, J. C. Watson, P. Bartlett, and F. Renzoni, "Electromagnetic imaging through thick metallic enclosures," *AIP Adv.*, vol. 5, no. 8, 2015, Art. no. 087143.

[8] Z. Zakaria *et al.*, "Advancements in transmitters and sensors for biological tissue imaging in magnetic induction tomography," *Sensors*, vol. 12, no. 6, pp. 7126–7156, May 2012.

[9] R. Liu, Y. Li, F. Fu, F. You, X. Shi, and X. Dong, "Time-difference imaging of magnetic induction tomography in a three-layer brain physical phantom," *Meas. Sci. Technol.*, vol. 25, no. 6, Jun. 2014, Art. no. 065402.

[10] Z. Xu, H. Luo, W. He, C. He, X. Song, and Z. Zahng, "A multichannel magnetic induction tomography measurement system for human brain model imaging," *Physiol. Meas.*, vol. 30, no. 6, pp. S175–S186, Jun. 2009.

[11] L. Marmugi and F. Renzoni, "Optical magnetic induction tomography of the heart," *Sci. Rep.*, vol. 6, no. 1, p. 23962, Jul. 2016.

[12] G. Hu, E. Cressman, and B. He, "Magnetoacoustic imaging of human liver tumor with magnetic induction," *Appl. Phys. Lett.*, vol. 98, no. 2, Jan. 2011, Art. no. 023703.

[13] X. Li, Y. Xu, and B. He, "Magnetoacoustic tomography with magnetic induction for imaging electrical impedance of biological tissue," *J. Appl. Phys.*, vol. 99, no. 6, Mar. 2006, Art. no. 066112.

[14] H. Scharfetter, H. K. Lackner, and J. Rosell, "Magnetic induction tomography: Hardware for multi-frequency measurements in biological tissues," *Physiol. Meas.*, vol. 22, no. 1, p. 131, 2001.

[15] S. Al-Zeibak and N. H. Saunders, "A feasibility study of *in vivo* electromagnetic imaging," *Phys. Med. Biol.*, vol. 38, no. 1, p. 151, 1993.

[16] M. Zolgharni, H. Griffiths, and P. D. Ledger, "Frequency-difference MIT imaging of cerebral haemorrhage with a hemispherical coil array: Numerical modelling," *Physiol. Meas.*, vol. 31, no. 8, pp. S111–S125, Aug. 2010.

[17] L. Wang and A. M. Al-Jumaily, "Imaging of lung structure using holographic electromagnetic induction," *IEEE Access*, vol. 5, pp. 20313–20318, 2017.

[18] S. R. Higson *et al.*, "Development of a sensor for visualization of steel flow in the continuous casting mould," *Revue de Metallurgie-Cahiers d'Informations Techn.*, vol. 100, no. 6, pp. 629–632, 2003.

[19] P. Gaydecki, S. Quek, G. Miller, B. T. Fernandes, and M. A. M. Zaid, "Design and evaluation of an inductive Q-detection sensor incorporating digital signal processing for imaging of steel reinforcing bars in concrete," *Meas. Sci. Technol.*, vol. 13, no. 8, pp. 1327–1335, Aug. 2002.

[20] H.-Y. Wei and M. Soleimani, "A magnetic induction tomography system for prospective industrial processing applications," *Chin. J. Chem. Eng.*, vol. 20, no. 2, pp. 406–410, Apr. 2012.

[21] B. J. Darrer, J. C. Watson, P. Bartlett, and F. Renzoni, "Magnetic imaging: A new tool for UK national nuclear security," *Sci. Rep.*, vol. 5, no. 1, p. 7944, Jul. 2015.

[22] A. Sophian, G. Y. Tian, D. Taylor, and J. Rudlin, "Electromagnetic and eddy current NDT: A review," *Insight*, vol. 43, no. 5, pp. 1–5, 2001.

[23] D. J. Pasadas, P. Baskaran, H. G. Ramos, and A. L. Ribeiro, "Detection and classification of defects using ECT and multi-level SVM model," *IEEE Sensors J.*, vol. 20, no. 5, pp. 2329–2338, Mar. 2020.

[24] A. Stubendekova and L. Janousek, "Impact of defect extent on swept frequency eddy current responses in non-destructive evaluation," *Electr. Eng.*, vol. 99, no. 4, pp. 1275–1281, Dec. 2017.

[25] A. Sophian, G. Tian, and M. Fan, "Pulsed eddy current non-destructive testing and Evaluation: A review," *Chin. J. Mech. Eng.*, vol. 30, no. 3, pp. 500–514, 2017.

[26] L. U. Daura, G. Y. Tian, Q. Yi, and A. Sophian, "Wireless power transfer-based eddy current non-destructive testing using a flexible printed coil array," *Philos. Trans. Roy. Soc. A*, vol. 378, no. 2182, 2020, Art. no. 20190579.

[27] Z. Z. Yu, A. J. Peyton, W. F. Conway, L. A. Xu, and M. S. Beck, "Imaging system based on electromagnetic tomography (EMT)," *Electron. Lett.*, vol. 29, no. 7, pp. 625–626, 1993.

[28] A. Korjenevsky, V. Cherepenin, and S. Sapetsky, "Magnetic induction tomography: Experimental realization," *Physiol. Meas.*, vol. 21, no. 1, pp. 89–94, Feb. 2000.

[29] J. Netz, E. Forner, and S. Haagemann, "Contactless impedance measurement by magnetic induction-a possible method for investigation of brain impedance," *Physiol. Meas.*, vol. 14, no. 4, pp. 463–471, 1993.

[30] C. H. Riedel, M. Keppelen, S. Nani, R. D. Merges, and O. Dössel, "Planar system for magnetic induction conductivity measurement using a sensor matrix," *Physiol. Meas.*, vol. 25, no. 1, pp. 403–411, 2004.

[31] H. Scharfetter, R. Marwa, and K. Pilz, "A new type of gradiometer for the receiving circuit of magnetic induction tomography," in *Proc. MIT 12th Int. Conf. Elec. Bio-Impedance V*, 2004, pp. 397–400.

[32] J. Rosell-Ferrer, R. Merwa, P. Brunner, and H. Scharfetter, "A multifrequency magnetic induction tomography system using planar gradiometers: Data collection and calibration," *Physiol. Meas.*, vol. 27, no. 5, pp. 271–280, 2006.

[33] B. U. Karbeyaz and N. G. Gencer, "Electrical conductivity imaging via contactless measurements: An experimental study," *IEEE Trans. Med. Imag.*, vol. 22, no. 5, pp. 627–635, May 2003.

[34] S. Watson, A. Morris, R. J. Williams, H. Griffiths, and W. Gough, "A primary field compensation scheme for planar array magnetic induction tomography," *Physiol. Meas.*, vol. 25, no. 1, pp. 271–279, 2004.
[35] C. H. Igney, S. Watson, R. J. Williams, H. Griffiths, and O. Dössel, "Design and performance of a planar-array MIT system with normal sensor alignment," *Physiol. Meas.*, vol. 26, no. 2, pp. 263–278, 2005.
[36] R. Eichardt, C. H. Igney, J. Kahlert, M. Hamsch, M. Vauhkonen, and J. Haueisen, "Sensitivity comparisons of cylindrical and hemispherical coil setups for magnetic induction tomography," in *Proc. IFMBE*, vol. 25, 2009, pp. 269–272.
[37] L. Du and J. Zhe, "Parallel sensing of metallic wear debris in lubricants using undersampling data processing," *Tribol. Int.*, vol. 53, pp. 28–34, Sep. 2012.
[38] L. Du, X. Zhu, Y. Han, L. Zhao, and J. Zhe, "Improving sensitivity of an inductive pulse sensor for detection of metallic wear debris in lubricants using parallel LC resonance method," *Meas. Sci. Technol.*, vol. 24, no. 7, 2013, Art. no. 075106.
[39] R. Guilizzoni, J. C. Watson, P. Bartlett, and F. Renzoni, "Imaging by electromagnetic induction with resonant circuits," *Proc. SPIE*, vol. 9481, May 2015, Art. no. 94810Q.
[40] R. Guilizzoni, J. C. Watsonb, P. A. Bartletta, and F. Renzonia, "Electromagnetic induction imaging of concealed metallic objects by means of resonating circuits," *Proc. SPIE*, vol. 9823, May 2016, Art. no. 98230P.
[41] L. Ma, H.-Y. Wei, and M. Soleimani, "Planar magnetic induction tomography for 3D near subsurface imaging," *Prog. Electromagn. Res.*, vol. 138, pp. 65–82, 2013.
[42] M. Ravan, R. K. Amineh, A. Hussein, O. Simanov, and A. Agarwal, "Electromagnetic induction imaging of metallic objects at multiple depths," *IEEE Magn. Lett.*, vol. 11, 2020, Art. no. 2100405.
[43] A. Rodriguez-Rivera, B. V. Baryshnikov, B. D. Vanveen, and R. T. Wakai, "MEG and EEG source localization in beamspace," *IEEE Trans. Biomed. Eng.*, vol. 53, no. 3, pp. 430–441, Mar. 2006.
[44] *LDC131x and LDC161x EVM User's Guide, Literature Number: SNOU135A*, Texas Instruments, Dallas, TX, USA, Sep. 2016. [Online]. Available: http://www.ti.com/lit/ug/snou135a/snou135a.pdf
[45] *LDC1312, LDC1314 Multi-Channel 12-Bit Inductance to Digital Converter (LDC) for Inductive Sensing*, Texas Instruments, Dallas, TX, USA, 2018. [Online]. Available: http://www.ti.com/lit/ds/symlink/ldc1312.pdf
[46] *LDC Reference Coils User's Guide, Literature Number: SNOU136*, Texas Instruments, Dallas, TX, USA, May 2015. [Online]. Available: http://www.ti.com/lit/ug/snou136/snou136.pdf
[47] Z. Wang, A. C. Bovik, H. R. Sheikh, and E. P. Simoncelli, "Image quality assessment: From error visibility to structural similarity," *IEEE Trans. Image Process.*, vol. 13, no. 4, pp. 600–612, Apr. 2004.
[48] S. Watson, R. J. Williams, W. Gough, and H. Griffiths, "A magnetic induction tomography system for samples with conductivities below 10 S m^{-1}," *Meas. Sci. Technol.*, vol. 19, no. 4, 2008, Art. no. 045501.
[49] D. M. Sheen, D. L. Mcmakin, and T. E. Hall, "Three-dimensional millimeter-wave imaging for concealed weapon detection," *IEEE Trans. Microw. Theory Techn.*, vol. 49, no. 9, pp. 1581–1592, Sep. 2001.
[50] R. K. Amineh, M. Ravan, A. Khalatpour, and N. K. Nikolova, "Three-dimensional near-field microwave holography using reflected and transmitted signals," *IEEE Trans. Antennas Propag.*, vol. 59, no. 12, pp. 4777–4789, Dec. 2011.
[51] R. K. Amineh, N. K. Nikolova, and M. Ravan, *Real-Time Three-Dimensional Imaging of Dielectric Bodies Using Microwave/Millimeter Wave Holography*. Hoboken, NJ, USA: Wiley, 2019.
[52] G. Y. Tian, Z. X. Zhao, R. W. Baines, and P. Corcoran, "Blind sensing [eddy current sensor]," *Manuf. Engineer*, vol. 76, no. 4, pp. 179–182, Aug. 1997.
[53] Y. Le Bihan, "Lift-off and tilt effects on eddy current sensor measurements: A 3-D finite element study," *Eur. Phys. J. Appl. Phys.*, vol. 17, no. 1, pp. 25–28, Jan. 2002.
[54] R. K. Amineh, M. Ravan, S. Sadeghi, and R. Moini, "Removal of probe liftoff effects on crack detection and sizing in metals by the AC field measurement technique," *IEEE Trans. Magn.*, vol. 44, no. 8, pp. 2066–2073, Aug. 2008.

Mahindra Ganesh received the M.Sc. degree in electrical and computer engineering from the New York Institute of Technology, New York, NY, USA, in 2020.

He has been a Research Assistant in the Applied Electromagnetics Research Laboratory, New York Institute of Technology since 2020. His research interests include applications of electromagnetics phenomena in imaging and power generation, quantum mechanics, hardware design, and prototyping of novel technologies.

Maryam Ravan (Senior Member, IEEE) received the Ph.D. degree from the Amirkabir University of Technology, Tehran, Iran.

She was a Post-Doctoral Fellow with the Departments of Electrical and Computer Engineering, University of Toronto, Toronto, ON, Canada, McMaster University, Hamilton, Canada, and Ryerson University, Toronto, Canada, from 2007 to 2013, where she was involved in solving forward modeling and inverse problems and the related signal/image processing techniques for biomedical, radar systems, microwave imaging, and nondestructive testing (NDT) applications. She was also a Lecturer with the School of Computational Engineering and Science, McMaster University, from 2009 to 2012. From 2013 to 2017, she was a Senior Research Scientist with the Department of Research and Development, LivaNova PLC, London, U.K., where her work focused on developing quantitative biomarkers and machine learning algorithms for investigating the efficacy of closed-loop Vagus nerve stimulation (VNS) therapy for epilepsy. She is currently an Assistant Professor with the Department of Electrical and Computer Engineering, New York Institute of Technology, New York, NY, USA. Her research interests include signal and image processing, beamforming, machine learning, microwave holography, MIMO radar systems and space time adaptive processing, and nondestructive testing. She has authored/coauthored over 70 journal and conference papers, a book chapter, and a book. Her research has been supported by US National Science Foundation (NSF), DND/NSERC Research Partnership Grant with Defense Research and Development Canada (DRDC) and Raytheon Canada Ltd, MITACS Internship with St. Joseph's Hospital in Hamilton, Canada, and NSERC Engage Grant with Raytheon Canada Ltd.

Reza K. Amineh (Senior Member, IEEE) received the Ph.D. degree in electrical engineering from McMaster University, Hamilton, Canada, in 2010.

He is currently an Assistant Professor with the Department of Electrical and Computer Engineering, New York Institute of Technology, New York, NY, USA. Prior to that, he was a Principal Scientist with the Department of Sensor Physics, Halliburton Co., Houston, TX, USA. He was a Post-Doctoral Fellow at the University of Toronto, Toronto, Canada, and McMaster University, from 2012 to 2013 and from 2010 to 2012, respectively. He was a Ph.D. Intern with the Advanced Technology Group, BlackBerry, in 2009. He has authored/coauthored over 80 journal and conference papers, two book chapters, and a book titled "Real-Time Three-Dimensional Imaging of Dielectric Bodies Using Microwave/Millimeter Wave Holography" published by Wiley & IEEE Press. He contributed to more than 40 patent disclosures in applied electromagnetics while working at Halliburton Co. and received several industrial awards. His research interests include applied electromagnetics with applications in imaging and sensing.

Dr. Amineh was a recipient of the Banting Post-Doctoral Fellowship from the Government of Canada in 2012 and the Ontario Ministry of Research and Innovation (OMRI) Post-Doctoral Fellowship in 2010. During his Ph.D. program, he was awarded the McMaster Internal Prestige Scholarship Clifton W. Sherman for two consecutive years. He has coauthored a paper selected as a finalist in the student paper competition at IEEE Wireless and Microwave Technology Conference in 2019, an Honorable Mention Paper presented at the IEEE Symposium on Antennas and Propagation in 2008, and a paper selected among the journal of Inverse Problems' "Highlights Collection of 2010."